ADVANCED SUSTAINABLE SYSTEMS
www.advsustainsys.com

Enhanced Solar CO_2 Photoreduction to Formic Acid by Platinum Immobilization on Bipyridine Covalent Triazine Framework with Defects

Kerem Kaya, Daniel Ditz, Aleksander Jaworski, Jianhong Chen, Susanna Monti, Giovanni Barcaro, Serhiy Budnyk, Adam Slabon, and Regina Palkovits**

The immobilization and structural analysis of platinum nanoparticles on a nitrogen-rich, bipyridine-containing covalent triazine framework (bpyCTF) having structural defects are disclosed by taking advantage of ^{15}N solid-state nuclear magnetic resonance measurements at natural ^{15}N isotope abundance and X-ray photoelectron spectroscopic analyses. The photocatalyst (Pt@bpyCTF) with structural defects reduces CO_2 to formic acid (FA) at a rate of 152 µmol $h^{-1}g^{-1}$ and a selectivity higher than 95% over CO and H_2 in water under simulated solar light. The presence of amine defects and the immobilization of Pt cause improvement in the photocurrent density and CO_2 capture capacity (≈8% by weight) despite the moderate surface area (0.54 cm^3 g^{-1})of the photocatalyst. Theoretical models and density functional theory calculations are employed to investigate the possible CO_2 reduction reaction (CO_2RR) mechanisms. Considering the exceptional CO_2 capture capacity and high FA production using only CO_2-bubbled water, this work highlights the great potential of nitrogen-rich CTFs for photocatalyzed CO_2RRs under green conditions.

1. Introduction

CO_2 emissions are mainly generated by the combustion of carbon-rich fossil fuels and contribute to global warming.[1,2] Mitigating global warming is considered to rely on future actions that will be taken to reduce CO_2 emissions. Despite the increasing number of renewable energy power plants, for example, wind, solar, hydroelectric, and biomass power, the global demand for carbon-based products continues to rise.[3] Recycled or not, all these products add up to the global CO_2 concentration.[4] It is therefore desirable to capture and transform the emitted CO_2 into useful chemicals under mild/ambient conditions in an energetically efficient manner.[5]

Considering the possible products of CO_2, it is thermodynamically and kinetically easier to reduce CO_2 into C1

K. Kaya
Department of Chemistry
Istanbul Technical University
Istanbul 34469, Turkey

K. Kaya
Department of Environmental Chemistry (MMK)
Stockholm University
Stockholm 10691, Sweden

D. Ditz
RWTH Aachen University
Institute of Technical and Macromolecular Chemistry
52074 Aachen, Germany

A. Jaworski, J. Chen
Department of Materials and Environmental Chemistry (MMK)
Stockholm University
Stockholm 10691, Sweden

The ORCID identification number(s) for the author(s) of this article can be found under https://doi.org/10.1002/adsu.202300071

DOI: 10.1002/adsu.202300071

S. Monti
CNR-ICCOM
Institute of Organometallic Compounds
Pisa 56124, Italy

G. Barcaro
CNR-IPCF
Institute of Chemical and Physical Processes
Pisa 56124, Italy

S. Budnyk
AC2T research GmbH
Wiener Neustadt 2700, Austria

A. Slabon
Chair of Inorganic Chemistry
University of Wuppertal
42119 Wuppertal, Germany
E-mail: slabon@uni-wuppertal.de

R. Palkovits
RWTH Aachen University
Institute of Technical and Macromolecular Chemistry
52074 Aachen, Germany
E-mail: Palkovits@itmc.rwth-aachen.de

R. Palkovits
Max-Planck Institute for Chemical Energy Conversion
45470 Mülheim an der Ruhr, Germany

products, such as carbon monoxide, formic acid (FA), methane, or methanol, instead of converting to higher carbon products, for example, ethanol, ethylene, acetic, and propanoic acids.[6–9] Among the C1 products, FA has been identified as a highly potent target of CO_2 reduction reaction (CO_2RR) that can be produced on a large scale.[10] FA is a valuable and safe chemical reagent with non-corrosive, eco-friendly properties.[11] It is mainly used in the leather/textile industry, pharmaceuticals, and food industry. Contrary to methanol which is another one-carbon product of CO_2RR, FA does not cross over the polymer membranes and is not causing blindness.[12] The annual global production of FA has reached 710 thousand tons with an annual market size of $1.6 billion (2021) and is expected to reach $3.85 billion by the year 2030.[13] Surprisingly, its volumetric capacity of hydrogen (4.3% by weight) surpasses that of most other well-known hydrogen storage chemicals. Due to its excellent oxidation kinetics, high cell potential, and limited fuel crossover problems,[14] FA has proven to be a promising hydrogen storage fuel that can empower future hydrogen fuel cell cars.[15]

Today, most of the FA is produced by thermochemical processes based on the carbonylation of methanol in basic media or by the oxidation of hydrocarbons.[16] All these chemical processes are associated with significant CO_2 emissions.[17–19] The use of solar light as the only source of energy input for CO_2RR to FA is a very desirable method to deal with increasing CO_2 emissions. Over the past 2 decades, research groups have designed and used homogeneous molecular catalysts, such as Ir, Ru, and Rh complexes, in conjunction with photosensitizers for light-driven CO_2RR to FA with high activity.[20–22] Nevertheless, the difficulty of recovering these costly catalysts from the reaction mixture, their poor photocatalytic stability, and the need for photosensitization invalidate the feasibility of these molecular catalysts for the production of FA on large scales.

Recently, nitrogen-rich covalent organic frameworks (COFs),[23–26] especially CTFs, have attracted augmented attention in CO_2RR due to their heterogeneous nature, high stability in various solvents including water, their large pore size, and their high surface area.[27–31] In addition, due to Lewis acid–base and dipole–quadrupole interactions between CO_2 and N-basic sites, CTFs can facilitate CO_2 adsorption.[32–36] CTFs with high CO_2 capture capacity hold high affinity to water, possibly due to the hydrogen bonding making these CTFs suitable catalysts for aqueous reactions.[37] In particular, pyridine-based CTFs can stabilize many metal nanoparticles (NPs) leading to basic materials, which are efficient for the activation of CO_2.[38,39] Introducing noble metal NPs, like PtNPs, on CTFs as co-catalyst usually improves the separation of photo-generated electron–hole pairs inhibiting rapid electron/hole recombination; a phenomenon which significantly lowers catalytic activity.[40,41] Previous studies have proven the crucial role of triethanolamine (TEOA) in the capture of ground-state CO_2 by binding to the metal center(s) present in the catalysts.[42] Findings have also shown that TEOA participates in the zwitterionic capture of CO_2.[43]

In light of the reports mentioned above, and inspired by previous works involving the use of a CTF for the hydrogen evolution reaction (HER) from water,[44,45] we aimed at synthesizing a photocatalyst system for the light-driven CO_2RR under mild conditions. Herein, we report using PtNPs immobilized in bipyridine containing CTF having structural defects as a photocatalyst (Pt@bpyCTF) for producing FA from CO_2 in water under simulated solar light and in conjunction with TEOA as a sacrificial electron donor under ambient conditions. The structure of Pt@bpyCTF was thoroughly investigated using diffractometric, microscopic, and spectral methods including ^{15}N CPMAS NMR at natural abundance. Control experiments suggest that the source of FA is CO_2, and the reaction does not proceed without the co-catalyst (PtNPs) or light. CO_2 reduction mechanisms at the hypothesized metal connection sites on the CTF structure were also investigated using representative models and density functional theory (DFT) calculations. In this study, we used ambient conditions (1 bar of CO_2 at room temperature) and water as the reaction medium (**Scheme 1**).

2. Results and Discussion

2.1. Synthesis and Structure of Pt@bpyCTF Catalyst

The formation of the covalent triazine rings was confirmed by IR (Figure S4, Supporting Information). The characteristic absorption peaks of the triazine ring at ≈1550 and 1300 cm^{-1} are due to C=N and C–N stretching vibrations, respectively, and indicate successful trimerization. The IR spectrum of Pt@bpyCTF shows no change in the functional groups and is nearly identical in the fingerprint region, which reveals that the immobilization of Pt-NPs did not affect the structural integrity of CTF.

^{1}H, ^{13}C, and ^{15}N CPMAS NMR spectra are shown in **Figure 1** together with chemical shifts calculated based on the model of the material. In the ^{1}H CPMAS NMR spectrum, the main resonance centered at 7.9 ppm originates from aromatic protons, whereas a much weaker signal at 4.2 ppm is attributed to protons of the $-NH_2$ groups that remain in the material after synthesis. This is probably due to the low degree of polymerization constituting certain structural defects in the framework. A weak signal in the 0–2 ppm region indicates small amounts of aliphatic protons. The observed carbon chemical shifts in the ^{13}C CPMAS NMR spectrum are in excellent agreement with those predicted for the model, which corroborates the material's chemical structure. Due to the low natural abundance of the ^{15}N isotope (less than 0.5%), low magnetogyric ratio (≈1/10 of that of ^{1}H) and the need for long spin–lattice relaxation times, direct observation of ^{15}N signals is most of the time not possible, thus, isotope enrichment is usually employed.[46–49] On the other hand, these limitations can be mitigated with the CPMAS[50] and DNP approaches.[51] We were able to obtain a high-quality ^{15}N CPMAS spectrum without using DNP and interpreted the obtained ^{15}N resonances with the help of quantum chemical calculations. In the ^{15}N CPMAS NMR spectrum, despite the two expected signals of pyridine and triazine nitrogen sites that exhibit NMR shifts of −72 and −128 ppm, respectively, an additional signal at −272 ppm is observed, which is assigned to $-NH_2$ groups, in agreement with the ^{1}H CPMAS NMR spectrum. Due to the severely broad distribution of ^{195}Pt isotropic chemical shifts as a consequence of the partially disordered nature of platinum environments in the nanoparticles,[52] no chemical information could be established from the recorded ^{195}Pt MAS NMR spectrum (see Figure S5, Supporting Information), in contrast to systems with distinct molecular/surface Pt environments.[53]

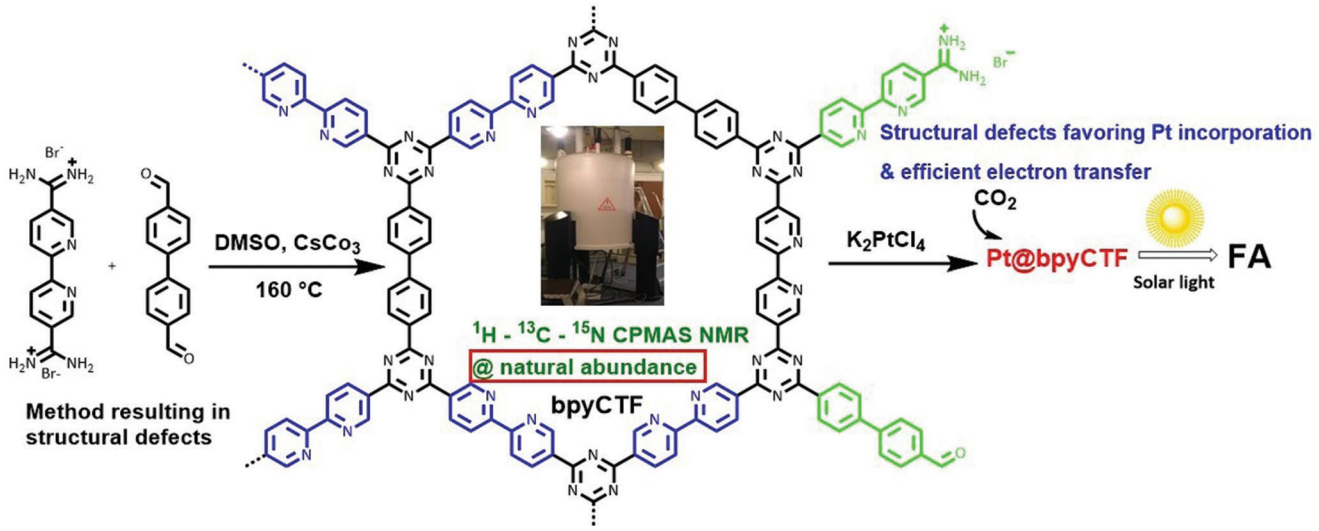

Scheme 1. Illustration and structural characterization of Pt@bpyCTF catalyzing CO_2RR under simulated solar light.

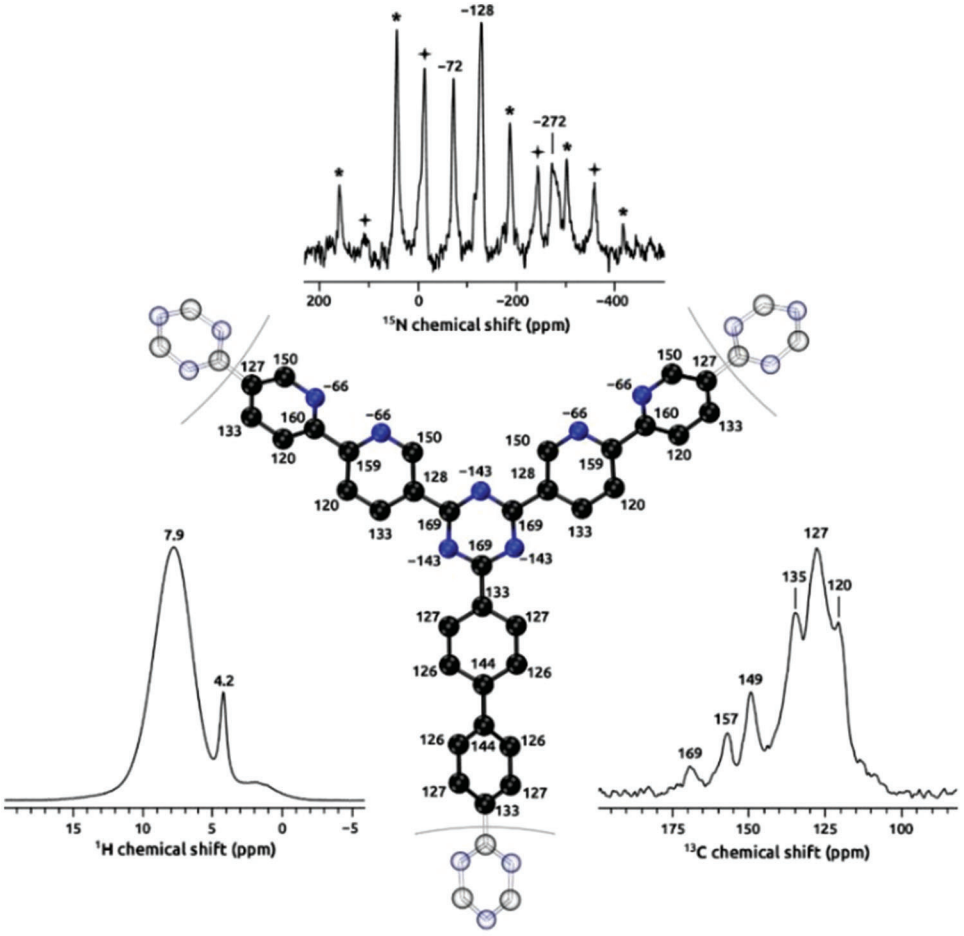

Figure 1. ^{1}H, ^{13}C, and ^{15}N CPMAS NMR spectra are shown together with chemical shifts calculated on the model of the material. Asterisks and stars denote spinning sidebands.

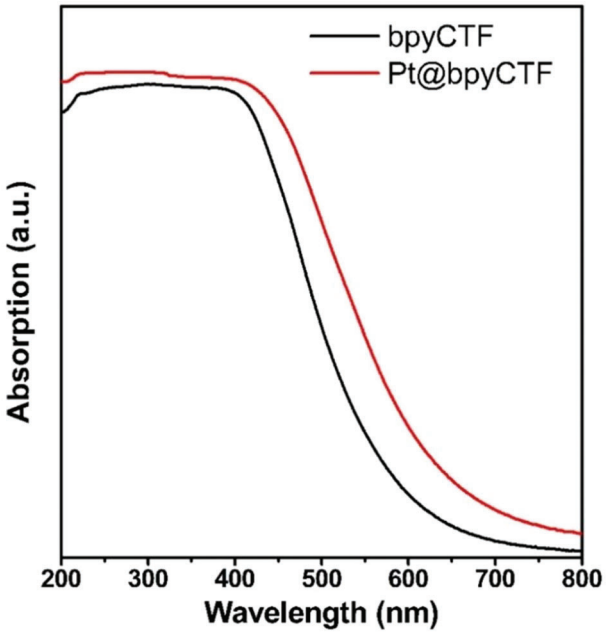

Figure 2. UV–vis diffuse reflectance spectra of pristine CTF (black) and Pt@bpyCTF (red).

The UV–vis diffuse reflectance spectra (DRS) of bpyCTF and Pt@bpyCTF were measured using $BaSO_4$ as background (**Figure 2**). Both compounds had excellent absorbance for the entire visible light region. It is possible to observe that the introduction of PtNPs caused a red shift (≈15 nm) of the absorption edge. This shift can be attributed to the formation of a Schottky contact at the Pt-bpyCTF interface associated with nitrogen defects, and consequently a shift in electron density.[54,55]

As expected, both materials hold more minor indirect transitions resulting in band gaps of 2.64 and 2.45 eV, for bpyCTF and Pt@bpyCTF, respectively (**Figure 3**). The corresponding direct band gaps, determined via the Tauc plot analysis confirm the smaller band gap for Pt@bpyCTF with 2.79 eV (445 nm) in comparison to the pristine material with 2.89 eV (430 nm). The noticeable difference between band gap and absorption onset (>750 nm for both materials), which is called Urbach tailing, indicates certain localized or mid-band gap states caused by the polydispersity and certain defects in the network.[56] It seems that the applied synthetic method plays a crucial role in the formation of these structural defects. It was previously demonstrated that such defects can act as catalytic centers which can facilitate the binding of metal co-catalysts and can give rise to different energy levels in the electronic band gap enabling photocatalytic activity at energies below the true electronic band gap.[57] Assuming that the oxidation potential equals the valence band maximum, which is separated by the band gap from the conduction band minimum (CBM), the resulting oxidation potentials are calculated as 2.72 V RHE for both bpyCTF and Pt@bpyCTF. (Figure S6, Supporting Information).

Actual Pt content in Pt@bpyCTF was determined by inductively coupled plasma optical emission spectroscopy (ICP-OES) as 2.58% by weight (Table S2, Supporting Information). Powder X-ray diffraction of both CTF and Pt@bpyCTF was measured to investigate the crystallinity of the compounds (Figure S7, Supporting Information). As expected both compounds were highly amorphous. Low-angle diffractions can be assigned to the in-plane reflections of the layered structure. The peak at ≈25° corresponding to a d-spacing of ≈3.9 Å is typical for the π–π stacked aromatic units explaining the amorphous nature of both compounds, observed in SEM images (Figure S8, Supporting Information).[58] No typical diffraction peak of Pt (111) could be observed at ≈39° indicates that Pt particles are small and well-dispersed within the triazine framework (Figure S9, Supporting Information). However, a new peak appearing at 27.5° can be attributed to the statistical positioning of Pt ions attached to amine groups in the mainframe of the crystal.[59]

bpyCTF yields a reduction potential of −0.14 V versus RHE which is reduced by 0.06 V through the incorporation of PtNP (0.08 V vs RHE). Flatband potentials were determined via Mott–Schottky analysis at the point of zero charge and the alignment

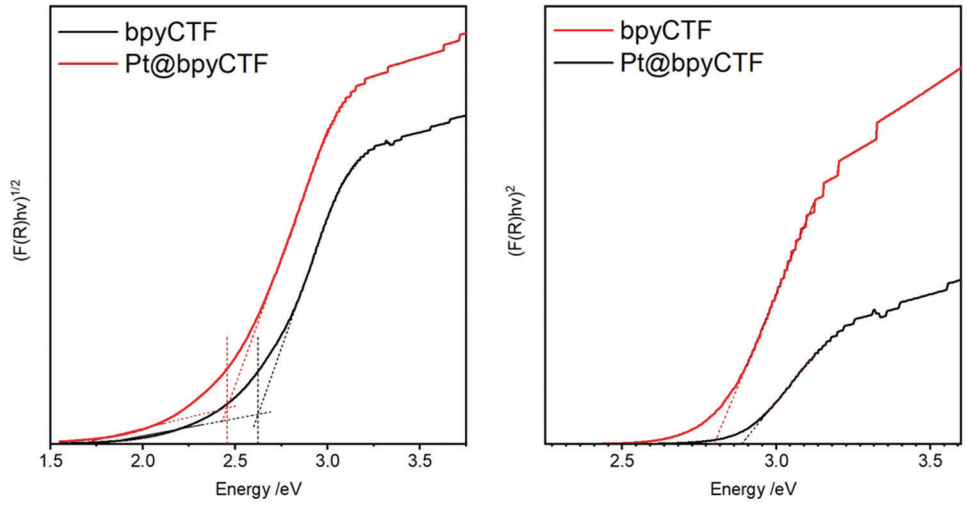

Figure 3. UV-Tauc plot for direct transitions (left) and indirect transitions (right) for CTF (black) and Pt@bpyCTF (red).

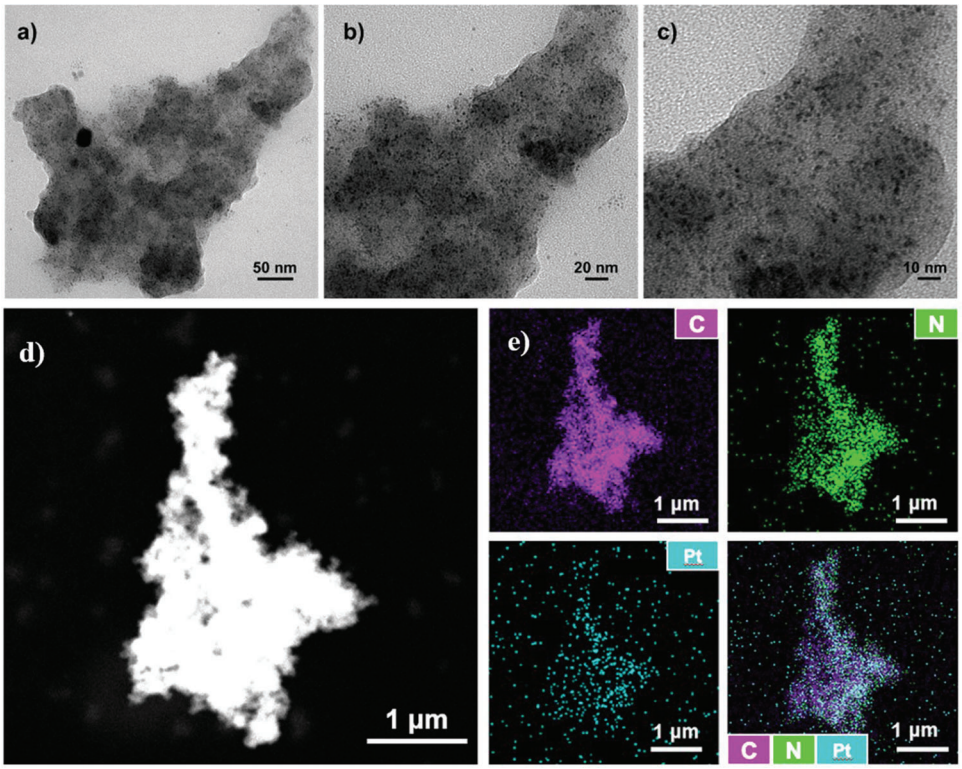

Figure 4. a–c) HR-TEM images (with different magnification), d) HAADF-STEM image, and e) EDX-mapping images (right) of Pt@bpyCTF.

of the redox potentials was based on the common assumption that the flat band lies close to the conduction band (Figure S10, Supporting Information).

Consequently, both materials should thermodynamically be able to oxidize TEOA, but their reduction potential looks insufficient to satisfy CO_2 reduction to either CO or FA, which contradicts the later discussed catalytic results. Zou et al. have recently demonstrated that flat-band analysis of nitrogen-rich CTFs might as well determine the mid-band gap states rather than the CBM.[60] In addition, it has been recently suggested that the defects in CTFs, such as dangling amine moieties, can positively affect the charge separation rendering the photocatalyst more active in reduction reactions and charge transfer via such defects (amine groups) might indeed cause better coordination to the Pt centers resulting in more efficient electron transfer due to amine-mediated proton-coupled electron transfer.[61,62] It was previously demonstrated that defects in 2D materials not only act as adsorption sites for CO_2 but also modulate the bandgap, thus decreasing the activation barrier in CO_2RR, leading to enhanced activity in photoreduction.[63,64] The photogenerated electrons localized mostly at the defect sites can provide a driving force to overcome the band gap energy for CO_2 reduction to FA (−0.70 V vs RHE) rather than that for HER (−0.10 V vs RHE).[65] This would be in line with our observed Urbach tail and explains why irradiation with >420 nm can result in excited states with higher reduction potential.

Transmission electron microscopy (TEM) images with different magnifications and energy-dispersive X-ray spectroscopy (EDX) elemental mapping images of Pt@bpyCTF can be seen in **Figure 4**. TEM images of Pt@bpyCTF in the figure (Figure 4a–c) reveal the presence of uniform and well-dispersed Pt nanoparticles throughout the material, with an average size of 2 nm. High-angle annular dark field (HAADF) scanning transmission electron microscopy (STEM) was used to gain further insight into the distribution of Pt nanoparticles within the material, as shown in Figure 4d. The HAADF-STEM and associated elemental mapping images (Figure 4e) provide information on the distribution of carbon (C), nitrogen (N), and platinum (Pt) within the material. All of the elemental mapping images show precise localization, indicating that Pt nanoparticles are uniformly distributed throughout the sample. This observation is consistent with the findings from the TEM images, suggesting that the Pt nanoparticles are well-dispersed within the material.

To unveil the charge-separation efficiency, photocurrent measurements were carried out for both compounds (**Figure 5**). Both materials showed a positive photocurrent, which is typical for n-type semiconductors. PtNPs on the bpyCTF surface led to a near quadrupling of the photocurrent, due to both Schottky contact and the structural defects. It is energetically favorable for the electrons to migrate into the PtNPs, which boosts exciton separation and reduces recombination. This can be attributed to possible Pt–N interaction between PtNPs and Pt ions and nitrogen of dangling amines and bpyCTF, respectively.[66]

To further demonstrate this assumption, X-ray photoelectron spectroscopy (XPS) was performed to analyze the interaction between Pt/N and the oxidation state(s) of Pt. N 1s peaks in bpyCTF shifted towards the high energy region by 0.4 eV in Pt@bpyCTF (**Figure 6**a). This could be attributed to the interaction between

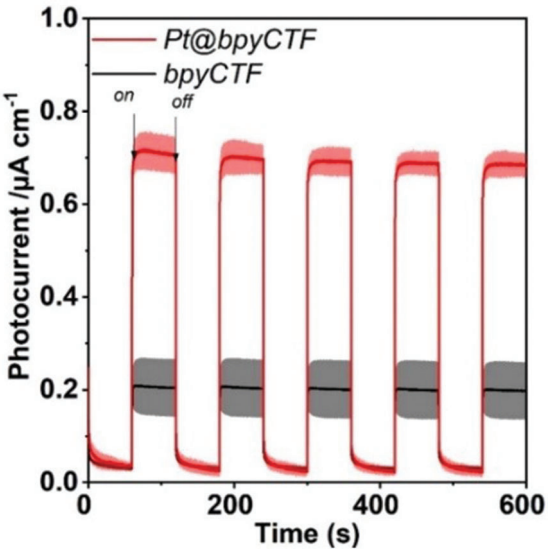

Figure 5. Photocurrent responses of bpyCTF (black) and Pt@bpyCTF (red) in a TEOA (17 vol%) solution in water under chopped UV light (365 nm).

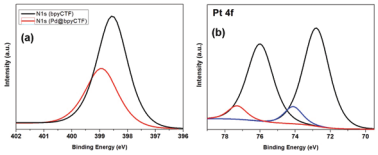

Figure 6. XPS spectra of a) N1s region of (black) bpyCTF and (red) Pt@bpyCTF b) Pt4f region of Pt@bpyCTF.

Pt and nitrogen of amine defects and bpyCTF.[67] In the high-resolution spectra of Pt 4 f (Figure 6b), the peaks at 75.9 ($Pt_{4f5/2}$) and 72.8 eV ($Pt_{4f7/2}$) are in good agreement with the zero valences of Pt, and the two small peaks with higher values (77.3 and 74.1 eV) can be assigned to Pt(II) species,[68] which more likely arises from the binding of Pt species to amine defects, the reoxidation of Pt (0) to Pt (II). Minor reoxidation of Pt (0) to Pt (II) can be attributed to the exposure of Pt (0) species to water resulting in the oxidation to Pt (II) as previously observed by other groups.[69,70] Further details about XPS measurements can be found in Figure S11, Supporting Information.

Brunauer–Emmett–Teller (BET) surface area and the total pore volume of bpyCTF and Pt@bpyCTF were studied by N_2 (Figure S12, Supporting Information) and CO_2 adsorption/desorption measurements (**Figure 7**). All the isotherms can be assigned as Type-I reversible isotherms, demonstrating the microporous nature of both bpyCTF and Pt@bpyCTF. The total pore volume of bpyCTF decreased from 0.79 to 0.54 $cm^3\ g^{-1}nm^{-1}$ after the immobilization of PtNPs. As expected, the nitrogen-rich characteristics of triazine and bipyridine groups result in a strong affinity for CO_2 and thereby high CO_2 adsorption capacity. Although there is a significant reduction (31.6%) in the pore size of Pt@bpyCTF compared with the pore size of bpyCTF, it shows even higher CO_2 capture capacity due to possible Lewis acid-base interaction between Pt species and adsorbed CO_2 molecules. These results confirmed the crucial role of Pt immobilization via structural defects in the CO_2 capture capacity.

Encouraged by the high CO_2 capture capacity, fast photocurrent response, and strong absorbance in the visible region of the electronic spectrum, the photocatalytic performance of Pt@bpyCTF was evaluated under visible light using TEOA as an electron/proton donor in pure water. The use of triethylamine (TEA) as the electron/proton donor resulted in a mixture of formaldehyde and FA, with a much lower amount of FA when compared to results obtained using TEOA (Figure S13, Supporting Information). After several trials using TEOA (Table S3, Supporting Information), the highest FA production rate was achieved by using 10 mg of photocatalyst in conjunction with 2 mL of TEOA after 8 h of irradiation (Figures S14–S16, Supporting Information). The main carbonaceous product in this system was detected as FA along with a trace amount of CO (2.5 ppm) as a side product (Figure S17, Supporting Information). H_2 was also detected (208 ppm) showing that HER, although minor, was present (Figure S18, Supporting Information). Previous DFT calculations suggested that co-adsorbed CO during HER significantly weakens the binding strength between H and the catalyst, especially, for metals on the right-hand side (too weak of hydrogen binding) leading to a suppression of the HER, as has been reported for metals such as Cu and Pt.[71] Control experiments were performed in the absence of CO_2, light, and PtNPs. It became clear that no FA was produced in the absence of light or PtNPs (Figure S19, Supporting Information). Successful recycling of the photocatalyst was also demonstrated by recovering the photocatalyst after the photoreaction, centrifuging, drying, and reusing it for additional photoreactions (Figures S20–S22, Supporting Information).

Considering the possible release of Pt atoms from the nanoparticles and their incorporation in bpyCTF (as suggested by the preliminary simulations, Figures S23 and S24, Supporting Information, we carried out), we investigated CO_2 reduction mechanisms at the hypothesized metal connection sites on the CTF structure using representative models and DFT calculations according to the computational details reported in the Supporting Information. We explored scenarios where the metal centers, which could be isolated atoms far from the PtNP (hence in a +2 oxidation state as observed in XPS data), or adatoms on the NP surface (where it is supposed a reduction to the 0 oxidation state, also observed in XPS) were chelated by the two nitrogen atoms of the bipyridine moiety, which seemed the most probable sites for the adsorption. Based on the experimental results, combined with the theoretical calculations and previous studies on photocatalytic CO_2 reduction over other complexes, we propose the possible steps of photocatalytic CO_2 reduction on the Pt@bpyCTF shown in **Figure 8**. As evidenced by the experiments and the simulated UV–vis absorption spectra of bipyridine (Figure S25, Supporting Information, red curve) and the ligand-metal adduct (Figure S25, Supporting Information, black line) in an aqueous solution, the inclusion of the metal center shows light absorption at about 560 nm in the visible light region due to the formation of a ligand-metal charge transfer complex. We could speculate that due to the trans effect in square-planar Pt complexes,[72] visible light excitation can induce the replacement of a water ligand with CO_2. Starting from this arrangement (Figure S26, Supporting Information, and related movies), where Pt is far from the NP surface, we simulated possible CO_2 to HCOOH reduction mechanisms, considering a water molecule and the sacrificial TEOA, by the Nudged Elastic

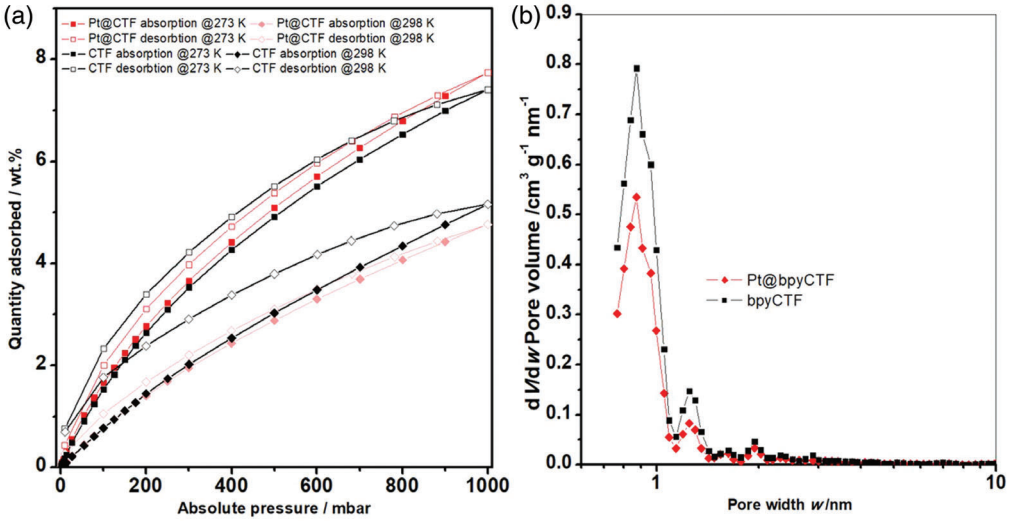

Figure 7. a) CO_2 adsorption–desorption isotherms b) pore size distributions of bpyCTF (black) and Pt@bpyCTF (red).

Band (NEB) approach. The identified transition structures were about 1.1 and 0.6 eV higher than the initial complex. The higher energy barrier corresponds to an H transfer to the carbon atom of CO_2, whereas the lower energy barrier to the transfer of the H of TEOA to one of the oxygen atoms of $HCOO^-$ (Figure S26, Supporting Information).

Similar reduction mechanisms can also be simulated on the surface of a PtNP by considering the adsorption of the Pt/bipyridine unit shown in Figure S24, Supporting Information, on a clean Pt (111) surface, as reported in Figure 8. Considering the water environment in which the reduction process takes place, we have explored two possible catalytic cycles. In the first cycle, the bare Pt catalyst, at the center of the square planar complex, is covered with two water molecules (state 1 of the purple path, top panel of Figure 8); whereas in the second one, only one water molecule is bound to the central Pt atom and the other position of the ligand is available for the adsorption of reacting species (state 1 of green path, bottom panel of Figure 8).

Reaction energies reported in **Figure 9** were calculated referring to gas-phase CO_2 and by adopting the hydrogen electrode method referring to standard conditions (pH = 0, $p(H_2) = 1$ bar, U = 0 V vs SHE)[73] to estimate a chemical potential of the H^+/e^- pairs. Inspecting the energy profiles, it can be seen that both cycles evolve according to a similar mechanism. Starting from the bare catalyst (state 1) and gas-phase CO_2, state 2 consists of the adsorption of CO_2 in the proximity of the catalytic system: CO_2* results more stable in the green path because of its interaction with the unsaturated Pt atom of the catalyst. State 3 foresees the first step of the reduction process, thanks to a hydrogen transfer from a water molecule of the catalyst to CO_2, forming the adsorbed COOH* in the purple case and HCOO* in the green case; the energy difference between states 2 and 3 in the green path is much higher (than in the other case) due to the lowest energy of 2 and to the largest energy needed to break the strong Pt–C bond. In state 4, a neutral H atom is adsorbed on the Pt atom of the catalyst next to the bipyridine unit, which can promote the coupling between an H^+ (donated by TEOA) and an electron (pushed from the excitation process), as previously investigated.[74]

In state 5, the incoming hydrogen is then transferred to the neighboring OH group in a highly exothermic process, restoring the catalyst to its native state. A second H addition followed by a second HAT (states 6 and 7, respectively) realize the complete reduction of HCOO*/COOH* and the formation of the final product, which, according to an endothermic process, can evolve into gas-phase formic acid. This last step is costly in the case of the purple path because of the strong stabilization of adsorbed formic acid (state 7), as also observed in previous work for very similar metal-organic catalysts.[75]

3. Conclusion

We have designed and characterized, via a variety of spectroscopic, microscopic, and computational techniques, a Pt@bpyCTF photocatalyst containing structural defects for the selective conversion of CO_2 to FA under ambient conditions, suggesting possible strategies to enhance the efficiency of this class of heterogeneous catalysts. The investigated system exhibited, in fact, excellent photocatalytic activity due to its highly unsaturated nitrogen environment and the presence of structural defects and Pt species, which increased both the photocurrent response and the CO_2 capture capacity (≈8% by weight). Multi-scale modeling based on RMD/QM simulations was used to shed light on the main steps characterizing photoreduction mechanisms, indicating the fundamental role synergically played by the organic matrix in contact with Pt atoms in both metallic and oxidized states. On a technical level, the presented results have demonstrated the potential of ssNMR spectroscopy to investigate a complex structure like bpyCTF using a straightforward and affordable technique, such as CP-MAS, without any isotope labeling. In particular, this allowed us to determine the structure of the covalent triazine network on the atomic level. We, therefore, believe that this advancement provides a unique opportunity to investigate the interface effects of COFs with metal nanoparticles.

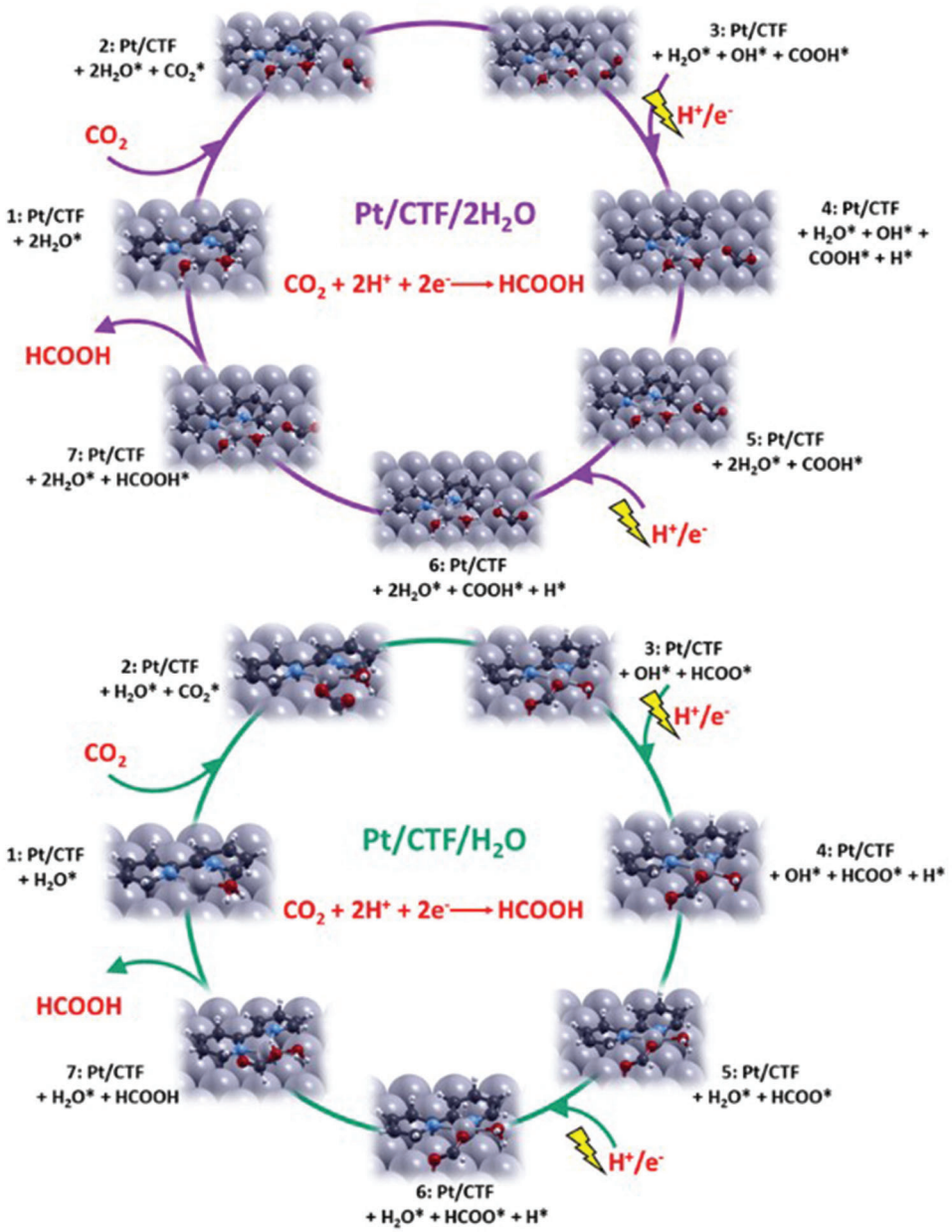

Figure 8. Photocatalytic reduction mechanisms of CO_2 for the Pt@bpyCTF system in water solution under visible light. Effect due to Pt (111) surface. Purple cycle (top): the bare Pt catalyst is at the center of a square planar complex and is covered with two water molecules; green cycle (bottom): only one water molecule is bound to the central Pt atom.

4. Experimental Section

IR Spectroscopy: IR absorption spectra were recorded using Varian Cary 4000 UV/VIS photospectrometer with an ATR accessory (ZnSe) and a mercury cadmium telluride (MCT) detector. A total of 32 scans were averaged.

NMR Spectroscopy: Magic-angle spinning (MAS) NMR experiments were performed at a magnetic field of 14.1 T (Larmor frequencies of 600.12, 150.92, and 60.83 MHz for ^{1}H, ^{13}C, and ^{15}N, respectively) on a Bruker Avance-III spectrometer. The ^{1}H MAS NMR spectrum was acquired using a 1.3 mm probehead and a 60 kHz MAS rate. It involved a rotor-synchronized, double-adiabatic spin-echo pulse sequence with a 90° excitation pulse of 1.25 µs followed by a pair of 50.0 µs tanh/tan short high-power adiabatic pulses (SHAPs) with 5 MHz frequency sweep.[1,2] All pulses operated at the nutation frequency of 200 kHz. 128 signal transients were acquired using a relaxation delay of 5 s. Cross-polarization (CP) ^{1}H-^{13}C and ^{1}H-^{15}N CPMAS NMR spectra were recorded using a 7 mm probe head employing a 7 kHz MAS rate and 65 kHz spinal64 pro-ton decoupling. For ^{1}H-^{13}C CPMAS acquisition, Hartmann–Hahn matched radiofrequency fields were applied for a contact interval of 1.5 ms, and 2048 signal transients were collected using a relaxation delay of 5 s. The ^{1}H-^{15}N CPMAS acquisition involved a contact interval of 5 ms and 16 384 scans collected with a relaxation delay of 5 s. Chemical shifts were referenced with respect to TMS (^{1}H, ^{13}C) and nitromethane (^{15}N). Calcula-

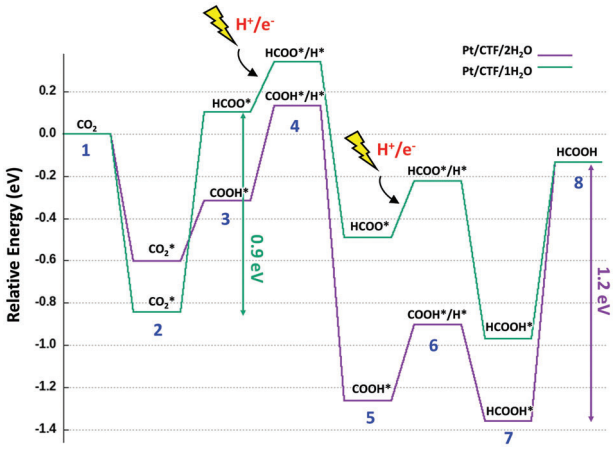

Figure 9. Energy profiles corresponding to the two different mechanisms depicted in Figure 8. Reaction energies were calculated referring to gas-phase CO_2 and by adopting the hydrogen electrode method in standard conditions (pH = 0, $p(H_2)$ = 1 bar, U = 0 V vs SHE).

tions of NMR shifts were performed with the ORCA code version 5.0.1.[3,4] Geometry of the model was optimized at the revPBE-D4/pcseg-1 level of theory[5–8] and NMR shieldings were subsequently calculated at the DSD-PBEP86/pcSseg-1 level of theory[9,10] with the GIAO approach[11] employing RIJCOSX approximation and the cc-pwCVDZ/C and def2/J auxiliary basis sets.[12–14] Calculated NMR shieldings were converted into isotropic chemical shifts using CH_4 and N_2 molecules in the gas phase as references.[15–18]

UV–vis Spectroscopy: UV–vis diffuse reflectance spectroscopy of the undiluted photocatalysts was measured with a UV 2600i spectrometer from Shimadzu with the respective accessory (ISR-2600 integrating sphere) in the range of 250 to 800 nm against BaSO4 as standard. The Shimadzu LabSolutions UV–vis-Software package was used for measurement control and data analysis. The band gap was determined via the Tauc-plot method for direct and indirect transitions.

Electrochemical and Photoelectrochemical Analysis: All (photo-) electrochemical measurements were performed with a three-electrode set-up from Metrohm (Autolab PGSTAT204), using a Pt counter electrode and an Ag/AgCl (3 M NaCl) reference electrode. The working electrode was fabricated by mixing under sonication 5 mg CTF (particle size <40 µm) with water, ethanol (50 µL each), and 1 wt% Nafion solution for 30 min. Then, 2 µL of the suspension was drop cast onto 0.25 cm^2 of an FTO substrate and dried under ambient conditions. The spare FTO surface was covered with an isolating paint. The sample was first conditioned via 25 CV cycles between 0.3 and 1.2 V (100 mV s^{-1}) before any analysis and the open circuit potential (OCP) was measured in the dark. Mott–Schottky measurements were conducted in the dark in Na_2SO_4 (2 M in water) electrolytes between −0.3 and 1.1 V in 0.05 V steps at three different frequencies (400, 700, and 1000 Hz). Prior, the isoelectric point was determined with a Malvern Panalytical Zetasizer Ultra equipped with an MPT-3 autotitrator via Zeta-potential measurements. Therefore, 10 mg CTF was sonicated for 1 h in 30 mL aqueous NaCl (10 mM in Milli-Q water, previously purged with argon), filtered through a 1.2 µm syringe filter and subsequently 15 mL were used for one Zeta-potential titration measurement. The pH was adjusted either to acidic or basic values using aqueous HCl (0.01 M) or aqueous NaOH (0.01 M) respectively, starting each time from the natural pH to minimize the salt loading. During the measurement, the solution was continuously purged with argon. The isoelectric point for both materials was around pH 4.5. Photocurrent measurements were performed in aqueous TEOA solution (17 vol%, natural pH) at OCP potential under periodical illumination from the back (60 s intervals, 365 nm, 1 W m^{-2}). All (photo-) electrochemical measurements were performed at least three times.

Physisorption Experiments: The ASAP 2060 device from micromeritics was used for N_2- and CO_2-physisorption experiments at 77 or 273 and 298 K, respectively. All samples were degassed at 150 °C before the measurement. The software MicroActive assisted data evaluation such as total pore volume determination, BET, and DFT modeling. Note that a DFT model developed was used here for rigid carbon with slit pore geometry (HS-2D-NLDFT, carbon, N_2@77 K), taking into account energetical heterogeny and geometrical corrugation of the carbon surface, but not considering any heteroatoms. As the CTFs contain a lot of heteroatoms (H, N), the pore size distributions obtained from the DFT model should be seen as a rough estimation. Single point total pore volume was obtained for the volume adsorbed at the relative pressure p/p0 = 0.95.

Induced Coupled Plasma Optical Emission Spectroscopy: Pt content was measured by ICP-OES (iCAP 7400 ICP-OES Duo, Thermo Fisher, Waltham, Massachusetts, USA). Prior to ICP-OES analyses, the representative samples taken were treated by acidic oxidative digestion in an Anton Paar Multiwave 3000 at 240 °C and 60 bar for 60 min.

Transmission Electron Microscopy: TEM images were obtained using an HT7800 TEM instrument equipped with a STEM and EDX module operating at 120 kV. Prior to the TEM measurements, the samples were dispersed in absolute ethanol solution using an ultrasonic bath for 1 h. The resulting dispersion was then deposited onto a carbon-coated copper grid and allowed to dry at room temperature.

Gas Chromatography: The gaseous products in the headspace of the Pyrex vessel were analyzed by gas chromatography (GC-7920A, Aulight Co., China) equipped with a flame-ionization detector (FID) to quantify CO and a thermal conductivity detector (TCD) to quantify H_2.

Quantification of FA: After 8 h of irradiation, 100 µL of DMF (internal standard) was added to the reaction mixture. The yield of FA was quantitatively determined by ^{1}H NMR Spectroscopy using 1 mL of the reaction mixture and 0.5 mL of deuterated water as the solvent against DMF internal standard.

Preliminary Investigations: Before investigating the mechanisms leading to the CO_2 reduction described by the experiments, reactive molecular dynamics (RMD) simulations (ReaxFF paradigm) were resorted to explore the complexity of the whole CTF/Pt system assembly in water solution and to identify the most probable events responsible for CO_2 entrapment and conversion. It was apparent from the experimental TEM characterization that the PtNPs did not display extended crystal facets that could host significant portions of the CTF in planar arrangements. Thus, possible representative supramolecular systems were built made of Pt clusters (two clusters of 266 atoms each, where the size was ≈2 nm), surrounded by a few (eight in all) CTF units (shown in Figure 1 of the manuscript) and water molecules (≈3500) (Figure S17, Supporting Information). The final simulation box was about 42 × 58 × 52 $Å^3$. Periodic boundary conditions were applied in all directions.

RMD simulations (ReaxFF methodology (van Duin, A. C. T.; Dasgupta, S.; Lorant F., Goddard III, W. A. J. Phys. Chem. A, 2001, 105, 9396–9409; Chenoweth, K.; van Duin, A. C. T.; Goddard III, W. A. J. Phys. Chem. A, 2008, 112, 1040–1053)), based on the force field used by D. Fantauzzi et al. (Fantauzzi D., Mueller J. E., Sabo L., van Duin A. C. T., Jacob t. ChemPhysChem, 2015, 16, 2797-2802) were carried out after energy minimization of the model and an initial equilibration in the NVT ensembled at ambient temperature and pressure (300 K and 1 atm). The production phase was about 300 ps. The stabilized structures where CTF chelated the Pt atoms, obtained at the end of the simulations, were extracted and used in the quantum chemistry optimizations and NEB simulations. In all the RMD runs, the time step was set to 0.2 fs, and the temperature was controlled through the Hoover–Nosé thermostat with a relaxation constant of 0.1 ps. RMDs were carried out with the ReaxFF code implemented in the Amsterdam Density Functional (ADF)/ReaxFF package (E. J. Baerends et al. ADF, adf2019.106 SCM, Theoretical Chemistry, Vrije Universiteit, Amsterdam, The Netherlands, http://www.scm.com).

Examination of the distance distribution functions shown in Figure S18, Supporting Information, indicates that water molecules and C and N atoms of the CTF units can be adsorbed on the PtNPs surface (strong interactions) and the portions of the chains in solution (or detached from the NP surface) can capture escaped Pt atoms. It can be speculated that the concerted action of the CTF and Pt in the various coordinated complexes

contributed effectively to the CO_2 reduction mechanisms. Thus, several reduced complexes of possible reaction mechanisms were prepared and performed quantum chemistry optimizations.

Structure Optimization and UV–vis Absorption Spectra: The models consisted of a bipyridine fragment, a Pt atom, a few explicit water molecules, and CO_2. These were optimized in water solution, represented through the Polarizable Continuum Model (CPCM), by means of the gaussian g09 software (g09 Revision C.01 Gaussian 09, Revision A.02, M. J. Frisch, G. W. Trucks, H. B. Schlegel, G. E. Scuseria, M. A. Robb, J. R. Cheeseman, G. Scalmani, V. Bar-one, G. A. Petersson, H. Nakatsuji, X. Li, M. Caricato, A. Marenich, J. Bloino, B. G. Janesko, R. Gomperts, B. Mennucci, H. P. Hratchian, J. V. Ortiz, A. F. Izmaylov, J. L. Sonnenberg, D. Williams-Young, F. Ding, F. Lipparini, F. Egidi, J. Goings, B. Peng, A. Petrone, T. Henderson, D. Rana-singhe, V. G. Zakrzewski, J. Gao, N. Rega, G. Zheng, W. Liang, M. Hada, M. Ehara, K. Toyota, R. Fukuda, J. Hasegawa, M. Ishida, T. Nakajima, Y. Honda, O. Kitao, H. Nakai, T. Vreven, K. Throssell, J. A. Montgomery, Jr., J. E. Peralta, F. Ogliaro, M. Bearpark, J. J. Heyd, E. Brothers, K. N. Kudin, V. N. Staroverov, T. Keith, R. Kobayashi, J. Normand, K. Raghavachari, A. Rendell, J. C. Burant, S. S. Iyengar, J. Tomasi, M. Cossi, J. M. Millam, M. Klene, C. Adamo, R. Cammi, J. W. Ochterski, R. L. Martin, K. Morokuma, O. Farkas, J. B. Foresman, and D. J. Fox, Gaussian, Inc., Wallingford CT, 2016), using DFT calculations with the Minnesota 06 Functional (M06-2X) functional. The 6–31G(d,p) basis set was used for all the elements except Pt which was described with the LANL2DZ basis set. The theoretical UV–vis absorption spectra in water solution were obtained using the time-dependent DFT (TD-DFT) method with the B3LYP functional and the same basis set employed for the geometry optimizations. For each complex, the first ten singlet excited states were used in the vertical excitation calculations.

Nudged Elastic Band Approach: To disclose possible minimum-energy paths (MEPs) for the CO_2RRs and estimate the activation energies (transition states -TS) that could be connected to the experiments, the NEB methodology (Sheppard, D.; Terrell, R.; Henkelman, G. J. Chem. Phys. 2008, 128, 134 106) implemented in the Quantum Espresso (Giannozzi, P.; Baroni, S.; Bonini, N.; Calandra, M.; Car, R.; Cavazzoni, C.; Ceresoli, D.; Chiarotti, G.; Cococcioni, M.; Dabo, I., et al. Quantum Espresso: A Modular and Open-Source Software Project for Quantum Simulations of Materials J. Phys.: Condens. Matter 2009, 21, 395 502) software package was used. The calculations were based on a plane-wave basis set; the projector augmented wave (PAW) method with Perdew–Burke–Ernzerhof (PBE) functional, and kinetic energy cutoffs of 40 and 400 Ry for the wave functions and the charge density, respectively. Single-particle wave functions were calculated through Gaussian smearing of 0.002 Ry. The Brillouin zone sampling was restricted to the gamma point, and all the calculations were spin-polarized. Long-range nonlocal effects were included by applying van der Waals corrections (Grimme-D2 approach). The energy barriers were estimated considering 15 intermediate images between the identified local minima, and a convergence cutoff of 0.05 eV $Å^{-1}$ for the force orthogonal to the path was employed. The geometry optimizations on the Pt (111) surface were carried out considering periodic boundary conditions and the computational details described above.

Synthesis of Monomers: The synthesis of monomers was done according to the (modified) literature procedure.

1) 5,5-Diamidine-2,2-dipyridyl dihydrobromide[19]

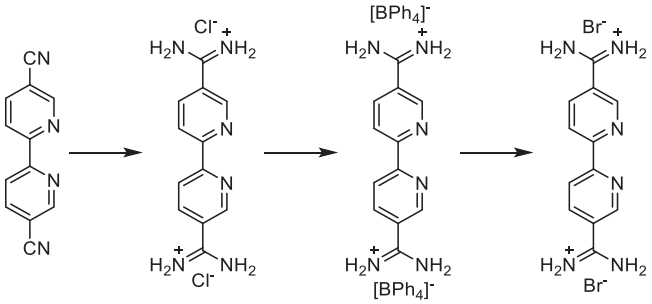

a) 5,5-Diamidine-2,2-bipyridine dihydrochloride

5,5-Dicyano-2,2-dipyridine (1 g, 5 mmol) was dissolved in dry THF (25 mL) under an argon atmosphere. $LiN(SiMe_3)_2$ in THF (1 M, 20 mL) was added dropwise at 0 °C. The resulting solution was stirred for 2 h at room temperature before it was cooled down again to 0 °C. The reaction was quenched by dropwise addition of HCl in EtOH (2 M, 200 mL) and the mixture was set aside overnight. Then, the precipitate was filtered, washed with EtOAc (3 × 100 mL) and THF (3 × 100 mL), and dried under vacuum. Yield: 751 mg, 2.40 mmol (48%). ^{1}H NMR (400 MHz, DMSO d6): δ = 9.70 (s, 4H, NH), 9.35 (s, 4H, NH), 9.15 (d, 2H, J = 2 Hz), 8.63 (d, 2H, J = 8 Hz), 8.45 (dd,2H, J = 8, JHH = 2.3 Hz);13C NMR (100 MHz; $CDCl_3$) δ = 163.6, 157.52, 149.1, 138.0, 125.4, 120.8;

b) 5,5-Diamidine-2,2-bipyridine ditetraphenylborate

5,5-Diamidine-2,2,-bipyridine dihydrochloride was dissolved in as little water as possible. Sodium tetraphenylborate (0.5 M in water) was added dropwise until no further precipitation could be observed. The white solid was filtered, washed with water, and dried under a vacuum. Yield: 2.065 g, 2.34 mmol (98%) ^{1}H NMR (400 MHz, DMSO d6): δ = 9.30 (br, 8H, NH), 9.11 (d, 2H, J = 2 Hz), 8.64 (d, 2H, J = 8 Hz), 8.40 (dd, 2H, J = 8.3 Hz, JHH = 2.3 Hz), 7.17 (s, 1H, ortho-H BPh_4), 6.92 (t, 2H, meta-H BPh_4, J = 7.3 Hz), 6.78 (t, 2H, para-H BPh_4, J = 7.1 Hz);

^{13}C NMR (100 MHz, DMSO d6) δ = 163.63, 163.38 (4 lines, 1JB-C = 49.3 Hz), 157.54, 149.03, 137.99, 135.56 (4 lines, 3JB-C = 1.3 Hz), 133.25, 126.25, 125.32, (4 lines, 2JB-C = 2.7 Hz), 121.54, 120.83; ^{11}B NMR (100 MHz, DMSO d6) δ = −6.69;

c) 5,5-Diamidine-2,2-bipyridine dihydrobromide

5,5-Diamidine-2,2-bipyridine ditetraphenylborate was dissolved in as little acetone as possible. Insoluble remains were separated via centrifugation. Then, tetrabutyl ammonium bromide (0.5 M in acetone) was added dropwise until no further precipitation was visible. The precipitate was filtered, and washed with acetone and EtOH before drying under a vacuum. Yield: 924 mg, 2.30 mmol (98%) 1H NMR (400 MHz, DMSO d6): δ = 9.40 (br, 8H, NH), 9.13 (d, 2H, J = 2.3 Hz), 8.64 (d, 2H, J = 8.3 Hz) 8.43 (dd, 2H, J = 8.3 Hz, J = 2.3 Hz); 13C NMR (100 MHz; DMSO d6) 164.01, 157.98, 149.50, 138.52, 126.02, 121.29;

Synthesis of Covalent Triazine Framework: The synthesis of bpyCTF was done according to a modified literature procedure.[20]

Supporting Information

Supporting Information is available from the Wiley Online Library or from the author.

Acknowledgements

All the authors contributed equally to this work. The manuscript was written through the contributions of all authors. All authors have given approval to the final version of the manuscript. A.S. acknowledges funding from Vinnova, Sweden's innovation agency (project: C1Bio, reference number 2019–03174). K.K. thanks the Olle Engkvists Stiftelse for a postdoctoral fellowship (213-0206). S.B. thanks the "Austrian COMET-Program" (project InTribology1, no. 872176) via the Austrian Research Promotion Agency (FFG) and the federal states of Niederösterreich and Vorarlberg, which was carried out within the "Excellence Centre of Tribology" (AC2T research GmbH). R.P. acknowledges the Fuel Science Center (EXC 3782186, ID: 390919832) funded by the Excellence Initiative by the German federal and state governments. D.D. gratefully thanks the German Federal Environmental Foundation for financial support. The authors thank Baris Yagci, Arda Baran Burcak, Tugser Yilmaz, and Zafer Eroglu for their help in XPS, PXRD, and TEM measurements.

Open access funding enabled and organized by Projekt DEAL.

Conflict of Interest

The authors declare no conflict of interest.

Data Availability Statement

The data that support the findings of this study are available from the corresponding author upon reasonable request.

Keywords

CO_2 reduction, covalent triazine frameworks, formic acid, photocatalysts, platinum nanoparticles, solar simulation

Received: March 6, 2023
Revised: April 17, 2023
Published online: May 17, 2023

[1] P. Gabrielli, M. Gazzani, M. Mazzotti, *Ind. Eng. Chem. Res.* **2020**, *59*, 7033.
[2] J. M. Ketzer, R. S. Iglesias, S. Einloft, In *Handbook of Climate Change Mitigation*, (Eds.: W.-Y. Chen, J. Seiner, T. Suzuki, M. Lackner), Springer US, New York **2012**, p. 1405.
[3] V. Sebestyén, *Renewable Sustainable Energy Rev.* **2021**, *151*, 111626.
[4] E. Billig, M. Decker, W. Benzinger, F. Ketelsen, P. Pfeifer, R. Peters, D. Stolten, D. Thrän, *J. CO2 Util.* **2019**, *30*, 130.
[5] N. Guntermann, H. G. Mengers, G. Franciò, L. M. Blank, W. Leitner, *Green Chem.* **2021**, *23*, 9860.
[6] H. Xiao, T. Cheng, W. A. Goddard, *J. Am. Chem. Soc.* **2017**, *139*, 130.
[7] I. Roh, S. Yu, C.-K. Lin, S. Louisia, S. Cestellos-Blanco, P. Yang, *J. Am. Chem. Soc.* **2022**, *144*, 8002.
[8] D. Kim, C. S. Kley, Y. Li, P. Yang, *PNAS* **2017**, *114*, 10560.
[9] C. Liu, B. E. Colón, P. A. Silver, D. G. Nocera, *J. Photochem. Photobiol., A* **2018**, *358*, 411.
[10] H. Yang, J. J. Kaczur, S. D. Sajjad, R. I. Masel, *J. CO2 Util.* **2020**, *42*, 101349.
[11] A. Kipshagen, J. C. Baums, H. Hartmann, A. Besmehn, P. J. C. Hausoul, R. Palkovits, *Catal. Sci. Technol.* **2022**, *12*, 5649.
[12] J. Guo, C. K. Yin, D. L. Zhong, Y. L. Wang, T. Qi, G. H. Liu, L. T. Shen, Q. S. Zhou, Z. H. Peng, H. Yao, X. B. Li, *ChemSusChem* **2021**, *14*, 2655.
[13] I. A. Zolotarskii, T. V. Andrushkevich, G. Y. Popova, S. Stompel, V. O. Efimov, V. B. Nakrokhin, L. Y. Zudilina, N. V. Vernikovskaya, *Chem. Eng. J.* **2014**, *238*, 111.
[14] M. Ramdin, A. R. T. Morrison, M. de Groen, R. van Haperen, R. de Kler, L. J. P. van den Broeke, J. P. M. Trusler, W. de Jong, T. J. H. Vlugt, *Ind. Eng. Chem. Res.* **2019**, *58*, 1834.
[15] J. Guo, C. K. Yin, D. L. Zhong, Y. L. Wang, T. Qi, G. H. Liu, L. T. Shen, Q. S. Zhou, Z. H. Peng, H. Yao, X. B. Li, *ChemSusChem* **2021**, *14*, 26551.
[16] A. K. M. L. Rahman, M. Kumashiro, T. Ishihara, *Catal. Commun.* **2011**, *12*, 1198.
[17] G. Tuci, A. Iemhoff, A. Rossin, D. Yakhvarov, M. F. Gatto, R. Balderas-Xicohténcatl, L. Zhang, M. Hirscher, R. Palkovits, C. Pham-Huu, G. Giambastiani, *Int. J. Hydrogen Energy* **2022**, *47*, 8434.
[18] F. M. Wisser, M. Duguet, Q. Perrinet, A. C. Ghosh, M. Alves-Favaro, Y. Mohr, C. Lorentz, E. A. Quadrelli, R. Palkovits, D. Farrusseng, C. Mellot-Draznieks, V. de Waele, J. Canivet, *Angew. Chem., Int. Ed.* **2020**, *59*, 5116.
[19] T. K. Todorova, T. N. Huan, X. Wang, H. Agarwala, M. Fontecave, *Inorg. Chem.* **2019**, *58*, 6893.
[20] A. Nakada, K. Koike, T. Nakashima, T. Morimoto, O. Ishitani, *Inorg. Chem.* **2015**, *54*, 1800.
[21] A. Rosas-Hernández, H. Junge, M. Beller, *ChemCatChem* **2015**, *7*, 3316.
[22] Y. Tamaki, T. Morimoto, K. Koike, O. Ishitani, *Proc. Natl. Acad. Sci. U. S. A.* **2012**, *109*, 15673.
[23] H. Lyu, H. Li, N. Hanikel, K. Wang, O. M. Yaghi, *J. Am. Chem. Soc.* **2022**, *144*, 12989.
[24] S. Yang, R. Sa, H. Zhong, H. Lv, D. Yuan, R. Wang, *Adv. Funct. Mater.* **2022**, *32*, 2110694.
[25] Y. Wang, Z. Hu, W. Wang, Y. Li, H. He, L. Deng, Y. Zhang, J. Huang, N. Zhao, G. Yu, Y.-N. Liu, *Appl. Catal., B* **2023**, *327*, 122419.
[26] L. Wang, L. Wang, S. Yuan, L. Song, H. Ren, Y. Xu, M. He, Y. Zhang, H. Wang, Y. Huang, T. Wei, J. Zhang, Y. Himeda, Z. Fan, *Appl. Catal., B* **2023**, *322*, 122097.
[27] A. V. Bavykina, E. Rozhko, M. G. Goesten, T. Wezendonk, B. Seoane, F. Kapteijn, M. Makkee, J. Gascon, *ChemCatChem* **2016**, *8*, 22171.
[28] H. Zhong, Z. Hong, C. Yang, L. Li, Y. Xu, X. Wang, R. Wang, *ChemSusChem* **2019**, *12*, 4493.
[29] G. Huang, G. Lin, Q. Niu, J. Bi, L. Wu, *J. Mater. Sci. Technol.* **2022**, *116*, 41.
[30] K. Park, G. H. Gunasekar, N. Prakash, K.-D. Jung, S. Yoon, *ChemSusChem* **2015**, *8*, 3410.
[31] A. Iemhoff, M. Vennewald, J. Artz, C. Mebrahtu, A. Meledin, T. E. Weirich, H. Hartmann, A. Besmehn, M. Aramini, F. Venturini, F. W. Mosselmans, G. Held, R. Arrigo, R. Palkovits, *ChemCatChem* **2022**, *14*, 202200179.
[32] H. Wang, D. Jiang, D. Huang, G. Zeng, P. Xu, C. Lai, M. Chen, M. Cheng, C. Zhang, Z. Wang, *J. Mater. Chem. A* **2019**, *7*, 228480.
[33] X. Zhu, C. Tian, G. M. Veith, C. W. Abney, J. Dehaudt, S. Dai, *J. Am. Chem. Soc.* **2016**, *138*, 11497.
[34] Y. Zhao, X. Liu, Y. Han, *RSC Adv.* **2015**, *5*, 30310.
[35] M. Lu, Q. Li, J. Liu, F.-M. Zhang, L. Zhang, J.-L. Wang, Z.-H. Kang, Y.-Q. Lan, *Appl. Catal., B* **2019**, *254*, 624.
[36] G. Tuci, M. Pilaski, H. Ba, A. Rossin, L. Luconi, S. Caporali, C. Pham-Huu, R. Palkovits, G. Giambastiani, *Adv. Funct. Mater.* **2017**, *27*, 1605672.
[37] C. Gu, D. Liu, W. Huang, J. Liu, R. Yang, *Polym. Chem.* **2015**, *6*, 7410.
[38] R. Luo, W. Xu, M. Chen, X. Liu, Y. Fang, H. Ji, *ChemSusChem* **2020**, *13*, 6509.
[39] S. Zhai, L. Zhang, J. Sun, L. Sun, S. Jiang, T. Yu, D. Zhai, C. Liu, Z. Li, G. Ren, *Front. Chem.* **2022**, *10*, 957412.
[40] G. Huang, Q. Niu, J. Zhang, H. Huang, Q. Chen, J. Bi, L. Wu, *Chem. Eng. J.* **2022**, *427*, 131018.
[41] K. Kamiya, R. Kamai, K. Hashimoto, S. Nakanishi, *Nat. Commun.* **2014**, *5*, 5040.
[42] C. Zhao, Z. Chen, R. Shi, X. Yang, T. Zhang, *Adv. Mater.* **2020**, *32*, 1907296.
[43] R. N. Sampaio, D. C. Grills, D. E. Polyansky, D. J. Szalda, E. Fujita, *J. Am. Chem. Soc.* **2020**, *142*, 2413.
[44] M. A. Fávaro, D. Ditz, J. Yang, S. Bergwinkl, A. C. Ghosh, M. Stammler, C. Lorentz, J. Roeser, E. A. Quadrelli, A. Thomas, R. Palkovits, J. Canivet, F. M. Wisser, *ACS Appl. Mater. Interfaces* **2022**, *14*, 14182.
[45] X. Hu, Z. Zhan, J. Zhang, I. Hussain, B. Tan, *Nat. Commun.* **2021**, *12*, 6596.
[46] R. Marek, A. Lycka, *Curr. Org. Chem.* **2002**, *6*, 35.
[47] I. Szewczyk, A. Rokicińska, M. Michalik, J. Chen, A. Jaworski, R. Aleksis, A. J. Pell, N. Hedin, A. Slabon, P. Kuśtrowski, *Chem. Mater.* **2020**, *32*, 7263.
[48] B. F. Chmelka, A. Pines, *Science* **1989**, *246*, 71.
[49] S. R. Chaudhari, P. Berruyer, D. Gajan, C. Reiter, F. Engelke, D. L. Silverio, C. Copéret, M. Lelli, A. Lesage, L. Emsley, *Phys. Chem. Chem. Phys.* **2016**, *18*, 10616.
[50] R. Jelinek, B. F. Chmelka, A. Stein, G. A. Ozin, *J. Phys. Chem.* **1992**, *96*, 6744.
[51] X. Li, I. V. Sergeyev, F. Aussenac, A. F. Masters, T. Maschmeyer, J. M. Hook, *Angew. Chem., Int. Ed.* **2018**, *57*, 6848.

[52] G. J. Rees, S. T. Orr, L. O. Barrett, J. M. Fisher, J. Houghton, G. H. Spikes, B. R. C. Theobald, D. Thompsett, M. E. Smith, J. V. Hanna, *Phys. Chem. Chem. Phys.* **2013**, *15*, 17195.
[53] A. Venkatesh, A. Lund, L. Rochlitz, R. Jabbour, C. P. Gordon, G. Menzildjian, J. Viger-Gravel, P. Berruyer, D. Gajan, C. Copéret, A. Lesage, A. J. Rossini, *J. Am. Chem. Soc.* **2020**, *142*, 18936.
[54] J. Li, P. Liu, Y. Tang, H. Huang, H. Cui, D. Mei, C. Zhong, *ACS Catal.* **2020**, *10*, 2431.
[55] Z. Zafar, S. Yi, J. Li, C. Li, Y. Zhu, A. Zada, W. Yao, Z. Liu, X. Yue, *Energy Environ. Mater.* **2022**, *5*, 68.
[56] J. Zhang, J. Chen, Y. Wan, H. Liu, W. Chen, G. Wang, R. Wang, *ACS Appl. Mater. Interfaces* **2020**, *12*, 13805.
[57] J. Di, C. Chen, C. Zhu, P. Song, J. Xiong, M. Ji, J. Zhou, Q. Fu, M. Xu, W. Hao, J. Xia, S. Li, H. Li, Z. Liu, *ACS Appl. Mater. Interfaces* **2019**, *11*, 30786.
[58] R. Gong, L. Yang, S. Qiu, W.-T. Chen, Q. Wang, J. Xie, G. I. N. Waterhouse, J. Xu, *Adv. Polym. Technol.* **2020**, *2020*, 7819049.
[59] S. Chen, P. Qi, J. Chen, Y. Yuan, *RSC Adv.* **2015**, *5*, 31566.
[60] Y. Zou, S. Abednatanzi, P. G. Derakhshandeh, S. Mazzanti, C. M. Schüßlbauer, D. Cruz, P. Van Der Voort, J. W. Shi, M. Antonietti, D. M. Guldi, A. Savateev, *Nat. Commun.* **2022**, *13*, 2171.
[61] P. M. Karthik, A. R. M. Shaheer, A. Vinu, B. Neppolian, *Small* **2019**, *16*, 1902990.
[62] F. Haase, T. Banerjee, G. Savasci, C. Ochsenfeld, B. V. Lotsch, *Faraday Discuss.* **2017**, *201*, 247.
[63] D. Maarisetty, R. Mary, D.-R. Hang, P. Mohapatra, S. S. Baral, *J. CO2 Util.* **2022**, *64*, 102175.
[64] J. Wu, Y. Huang, W. Ye, Y. Li, *Adv. Sci.* **2017**, *4*, 1700194.
[65] M. I. Hossain, J. D. Cunningham, T. M. Becker, B. E. Grabicka, K. S. Walton, B. D. Rabideau, T. G. Glover, *Chem. Eng. Sci.* **2019**, *203*, 346.
[66] Y. Injongkol, R. Intayot, N. Yodsin, A. Montoya, S. Jungsuttiwong, *Mol. Catal.* **2021**, *510*, 111675.
[67] L. Zhang, Y. Zhang, X. Huang, Y. Bi, *Chem. Sci.* **2022**, *13*, 8074.
[68] M. Liu, X. Wang, J. Liu, K. Wang, S. Jin, B. Tan, *ACS Appl. Mater. Interfaces* **2020**, *12*, 12774.
[69] Y. Zhao, P. V. Kumar, X. Tan, X. Lu, X. Zhu, J. Jiang, J. Pan, S. Xi, H. Y. Yang, Z. Ma, T. Wan, D. Chu, W. Jiang, S. C. Smith, R. Amal, Z. Han, X. Lu, *Nat. Commun.* **2022**, *13*, 2430.
[70] L. Liu, D. M. Meira, R. Arenal, P. Concepcion, A. V. Puga, A. Corma, *ACS Catal.* **2019**, *9*, 10626.
[71] L. Tan, S.-M. Xu, Z. Wang, Y. Xu, X. Wang, X. Hao, S. Bai, C. Ning, Y. Wang, W. Zhang, Y. K. Jo, S.-J. Hwang, X. Cao, X. Zheng, H. Yan, Y. Zhao, H. Duan, Y.-F. Song, *Angew. Chem., Int. Ed.* **2019**, *58*, 11860.
[72] Z. Chval, M. Sip, J. V. Burda, *J. Comput. Chem.* **2008**, *29*, 2370.
[73] J. K. Nørskov, J. Rossmeisl, A. Logadottir, L. Lindqvist, J. R. Kitchin, T. Bligaard, H. Jónsson, *J. Phys. Chem. B* **2004**, *108*, 17886.
[74] Y. Zheng, Y. Jiao, Y. Zhu, L. H. Li, Y. Han, Y. Chen, A. Du, M. Jaroniec, S. Z. Qiao, *Nat. Commun.* **2014**, *5*, 3783.
[75] M.-C. Hsieh, R. Krishnan, M.-K. Tsai, *Catalysts* **2022**, *12*, 890.